# Partial Gap Transduced MEMS Optoacoustic Oscillator Beyond Gigahertz

Siddharth Tallur, *Student Member, IEEE*, and Sunil A. Bhave, *Senior Member, IEEE*

***Abstract*— Electrostatically actuated microelectromechanical system (MEMS) oscillators are limited to few megahertz–gigahertz range on account of transduction inefficiency at higher frequencies. Piezoelectric transduction affords lower motional impedances at high frequencies, however mass-loading on account of metal electrodes imposes practical limits on the mechanical quality factor of piezoelectric resonators in the gigahertz frequency regime. In this paper, we present a silicon optoacoustic oscillator operating at 2.05 GHz with signal power 18 dBm and phase noise −80 dBc/Hz at 10-kHz offset from carrier. We employ displacement amplification and partial air gap capacitive transduction to enhance the transduction efficiency. An unconventional photolithography step is performed on a released MEMS structure, which greatly simplifies the fabrication process and allows electrical contact with the electrodes. Built-in nonlinear optomechanical modulation provides noiseless up-conversion of the oscillation signal all the way up to 16.4 GHz with −45-dBm signal power. We develop a phase noise model for the oscillator and identify the photodetector shot noise to be the dominant noise source. Using a high gain and low noise avalanche photodetector enables reduction of the far-from-carrier phase noise floor by 15dB. The phase noise model provides insights into understanding the influence of laser detuning on the oscillator noise performance, which has not been studied to date. [2013-0291]**

***Index Terms*— Opto-acoustic oscillator, phase noise, displacement amplifier, atomic layer deposition (ALD).**

## I. Introduction

DIRECT CONVERSION radio architectures require oscillators operating at GHz rate frequencies with good phase noise performance. MEMS-based oscillators fill the application gap between high-performance non-CMOS compatible quartz technology on the one hand, and low performance CMOS compatible LC oscillators on the other hand. Recently, our group developed a novel opto-acoustic oscillator [1] that employs photonic modulation of laser light coupled to a vibrating MEMS structure to sense displacements, that opens up avenues to scale frequencies of MEMS oscillators to the microwave X-band. The electrical performance of the best MEMS oscillators reported to date rivals the performance of typical quartz oscillators while allowing for higher levels of system and package integration than what is possible with present day quartz technology [2], [3]. Oscillators based on electrostatically transduced MEMS resonators have been demonstrated in the MHz frequency range [4], [5]. At higher frequencies, the motional impedance of electrostatically transduced resonators is large, and parasitic feedthrough does not yield a phase transition through 0° for the mechanical resoannce. Hence it is difficult to operate such a resonator in a feedback loop as an oscillator. Partial air gap transduction using atomic layer deposition (ALD) of various dielectrics has been explored to reduce the motional impedance [6]–[8], but oscillators operating beyond 1GHz have not been reported. Piezoelectric transduction presents lower motional impedances at these frequencies, and piezoelectrically transduced Film Bulk Acoustic wave Resonator (FBAR) [9]–[11] and Contour Mode Resonator (CMR) [12], [13] based oscillators operating at few GHz frequencies have been demonstrated. Scaling these piezoelectric oscillators to multi-GHz frequencies necessitates a thinner aluminum nitride film, which leads to mass-loading of the resonator due to the metal electrodes atop used to drive motion. This reduces the $k_t^2 - Q_{mech}$ (electromechanical coupling constant-mechanical quality factor product) for these resonators.

Advances in the photonics community has led to the development of the opto-electronic oscillator [14] which constitutes a delay line oscillator relying upon large optical delay in the signal path to achieve low phase noise. Our group has adapted this design into a MEMS structure by designing and operating an acousto-optic modulator in a feedback loop to realize an opto-acoustic oscillator (OAO) and GHz rate mechanical oscillations using this transduction scheme have been achieved [15]. The acousto-optic modulator combines the high quality factor filter response of the mechanical resonator with optical intensity and frequency modulation [16] obtained from an optical modulator. We have leveraged the high displacement sensitivity of optical resonances to sense mechanical motion at frequencies all the way up to 9.8GHz [17]. However the device suffers from inefficient electrostatic transduction at frequencies beyond 1GHz [15], [17] and does not qualify as a suitable candidate for designing a higher frequency oscillator.

This paper explores and demonstrates two innovations to the coupled-ring resonator based opto-acoustic oscillator (OAO) design to target higher frequencies. The first innovation is to use a micro-mechanical displacement amplifier [18] to achieve larger optical modulation. The second innovation is to use partial air gap capacitive transduction

Manuscript received September 16, 2013; revised June 14, 2014; accepted June 19, 2014. Date of publication July 8, 2014; date of current version March 31, 2015. This work was supported in part by the Defense Advanced Research Projects Agency/Microsystems Technology Office's Optical Radiation Cooling and Heating in Integrated Devices Program, in part by the Cornell Nanoscale Science and Technology Facility, and in part by the National Nanotechnology Infrastructure Network. Subject Editor C. T.-C. Nguyen.

The authors are with the OxideMEMS Laboratory, Cornell University, Ithaca, NY 14853 USA (e-mail: sgt28@cornell.edu; sunil@ece.cornell.edu).

Color versions of one or more of the figures in this paper are available online at http://ieeexplore.ieee.org.

Digital Object Identifier 10.1109/JMEMS.2014.2332495

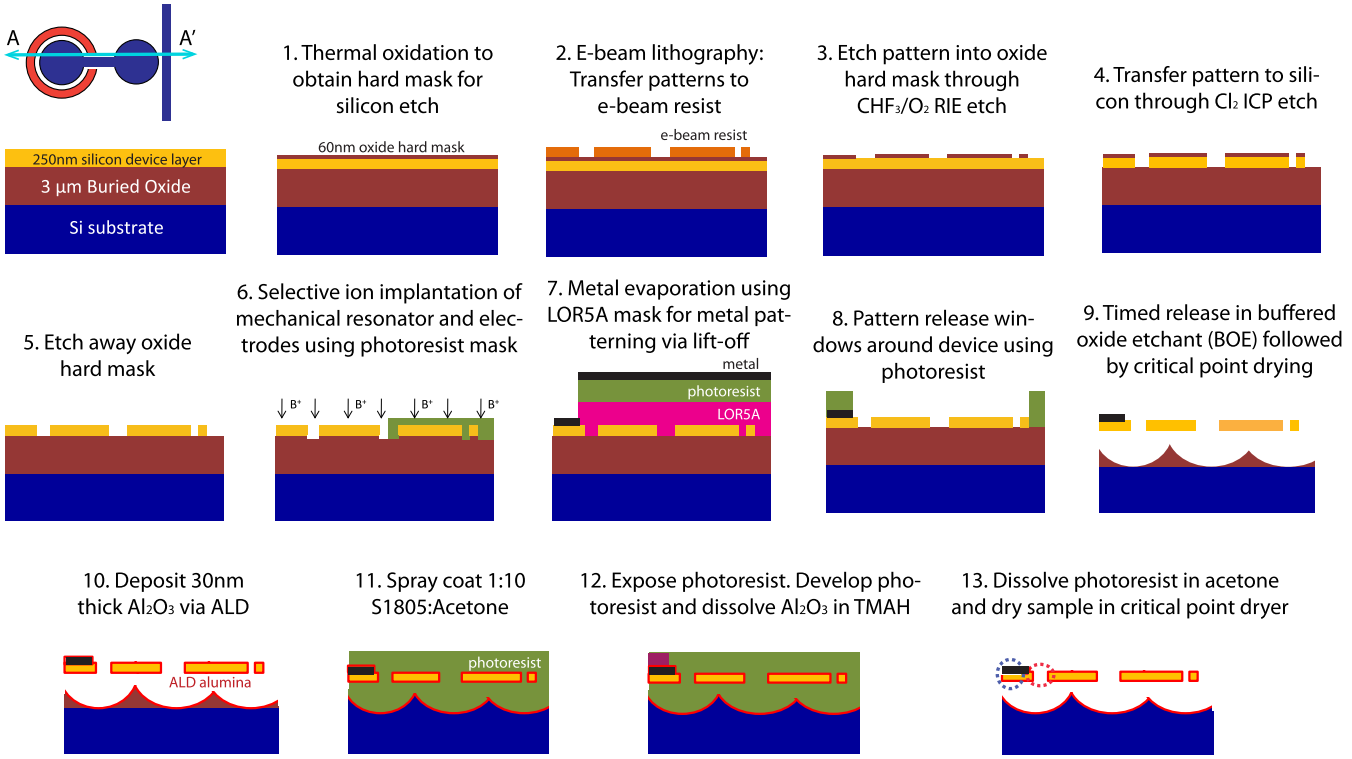


Fig. 1. Process flow to fabricate a silicon OAO. Steps 1 through 13 depict a cross-sectional profile of the wafer at the A-A' interface shown in the top left corner of the figure. The red and blue ellipses in step 13 show the reduced electrode-resonator air gap and the removal of alumina over the bond pad respectively.

to enhance the electromechanical transduction efficiency at higher frequencies. This is enabled using a novel process flow that employs photolithography on a released MEMS structure. We incorporate these ideas into the resonator design to demonstrate an electrostatically actuated silicon OAO operating at 2.05GHz. The oscillator has phase noise of $-80$dBc/Hz at 10kHz offset from the carrier. The non-linearity of the optical sense scheme generates multiple oscillation harmonics all the way up to 16.4GHz. We isolate the second and third harmonics of the oscillation signal at 4.1GHz and 6.15GHz and measure phase noise of these oscillation signals to be $-74$dBc/Hz and $-70$dBc/Hz respectively at 10kHz offset from carrier. We identify the shot noise in the photodetector to be the primary source of noise in the oscillator, and design a lower phase noise oscillator at 2.05GHz using a high gain, low noise avalanche photodetector that achieves a reduction in the noise floor by 15dB.

## II. Fabrication of the OAO

Figure 1 shows an illustration of the fabrication process flow. We choose a displacement amplifier array design for the modulator presented in [16]. Each individual ring in the array has a width of $3.8\mu m$, which corresponds to a fundamental compound radial mode frequency of 1.1GHz. Fabricating the modulator involves a five mask process flow on a custom silicon-on-insulator (SOI) wafer (undoped 250 nm device layer for low optical loss and $3\mu m$ thick buried oxide for isolation of the waveguides on device layer from the silicon substrate). The top silicon is thermally oxidized to obtain a thin oxide hard mask layer of thickness 60nm atop a 220nm thick silicon device layer. ma-N 2403 electron beam resist is spun on top of the oxide and patterned using electron beam lithography. The patterns are transferred into the silicon dioxide using a $CHF_3/O_2$ based reactive ion etcher and then into the silicon device layer using a chlorine based reactive ion etch. A layer of SPR-220 3.0 photoresist is spun and a second mask is used to pattern windows above the mechanical resonator, the electrical routing beams and the bond-pads. This is followed by a boron ion implantation and nitrogen anneal to reduce the resistivity of these structures. A third mask is then used to deposit metal over the bond pads for electrical contact. A layer of LOR-5A followed by a layer of SPR-220 3.0 is spun and the bond pads are exposed via contact alignment photolithography. This is followed by evaporation of 25nm nickel on the sample. Nickel forms a good ohmic contact with silicon, and is hence chosen as the bottommost metal. After evaporating nickel, we evaporate 25nm titanium and 50nm platinum. Platinum is used as the top metal as it makes good electrical contact with the Cascade Air Coplanar Probe (ACP) RF probe used to interrogate these devices. However platinum does not adhere well to nickel, and hence titanium is used as an adhesion layer. The photoresist is dissolved in Microposit remover solvent 1165 to leave metal only atop bond-pads. A fourth mask is used to pattern release windows near the resonator using SPR-220 3.0 photoresist, followed by a timed release etch in buffered oxide etchant to undercut the devices. The samples are then dried using a critical point

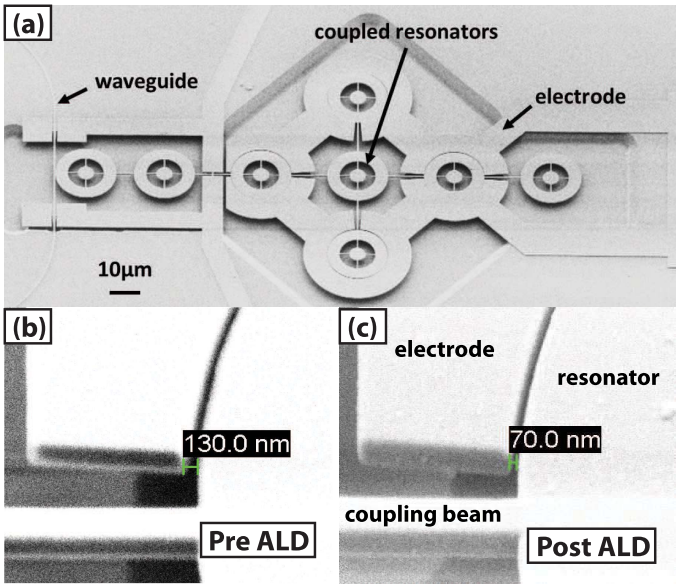


Fig. 2. (a) Scanning electron micrograph (SEM) of the displacement amplifier based partial air gap capactively transduced silicon acousto-optic modulator. The resonator-electrode gap is reduced from (b) 130nm prior to ALD to (c) 70nm post ALD.

dryer to prevent stiction. The released devices are transferred into an ALD chamber and the entire sample is blanket coated with 30nm alumina ($Al_2O_3$). Alumina is chosen because of its high dielectric constant (9.1) and because it dissolves easily in tetramethylammonium hydroxide (TMAH), which is also the chemical used for developing the photoresist. Following this step we spray coat the devices with $6\mu m$ thick diluted photoresist (1:10 S1805:Acetone). This is done because spin coating photoresist on a sample with released resonators will result in breakage of resonators from their anchors due to shear force. Also, a thick photoresist layer protects the devices from being damaged in the subsequent photolithography step used to pattern windows over the bond-pads. Developing the photoresist after exposure also results in etching away of the alumina covering the bond-pads and hence provides electrical access to the device. Choosing alumina as the ALD material does away with an extra etch step and thereby does not add extra complexity to the process flow. After stripping the photoresist in acetone, the sample is dried using a critical point dryer. The blue ellipse in step 13 of Figure 1 shows the opening on the bond-pad and the red ellipse shows the air gap reduction by lateral coverage of the resonator and electrode sidewalls with alumina. Figure 2(a) shows a scanning electron micrograph (SEM) of the fabricated device. Narrowing of the resonator-electrode gap from 130nm (Figure 2 (b)) to 70nm (Figure 2 (c)) after ALD is clearly seen in the SEM.

## III. Acousto-Optic Modulator

### A. Optical Characterization

We measure the optical response of the modulator prior to and post ALD. Light from a Santec TSL-510 tunable diode laser is coupled into the on-chip waveguide through grating couplers and the transmitted power is measured using an optical power meter. Figure 3 (a) shows the enhanced

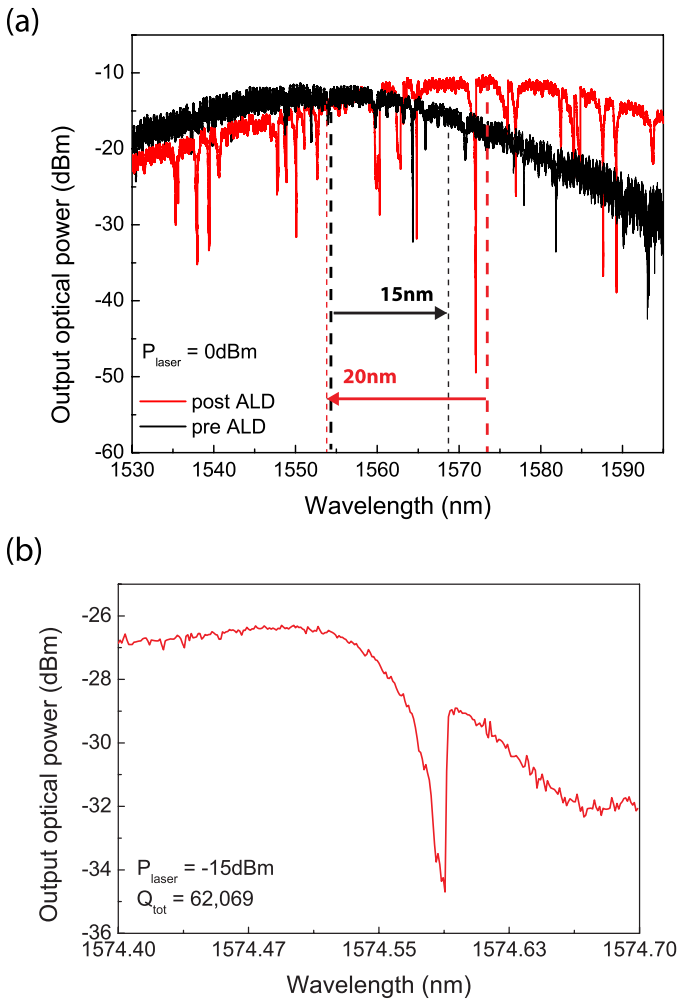


Fig. 3. (a) Optical transmission spectrum highlighting increase in grating transmission and bandwidth post ALD. The half-width-at-half-maximum bandwidth for the grating couplers increases from 15nm to 20nm. (b) High optical Q resonance for the device coated with 30nm alumina. The total (loaded) optical quality factor of the cavity is ≈62,000.

optical performance for the modulator post ALD. The grating transmission is boosted by 3dB, and the half-width-at-half-maximum bandwidth of the gratings increases from 15nm to 20nm. We choose a high optical loaded (total) quality factor ($Q_{tot}$) resonance at 1574nm shown in Figure 3 (b). The ALD step does not degrade the optical Q. The dip in the optical transmission spectrum in Figure 3 (b) at 1574.635nm is attributed to Fabry-Perot like resonances of the grating couplers used to couple light from the optical fiber into the on chip waveguide. The "shark-fin" ressonance shape is attributed to heating of the cavity on account of optical absorption, as the laser wavelength is swept into resonance. This heating causing an increase in the resonance wavelength thus resulting in a "shark-fin" resonance shape, similar to the duffing curves observed for mechanical resonators when driven into non-linear regime of operation.

As seen in Figure 3 (b), the ALD coating atop the waveguide and resonator enables coupling to a large number of optical resonances as compared to light coupling to few resonances obtained without ALD. This is attributed to the increased

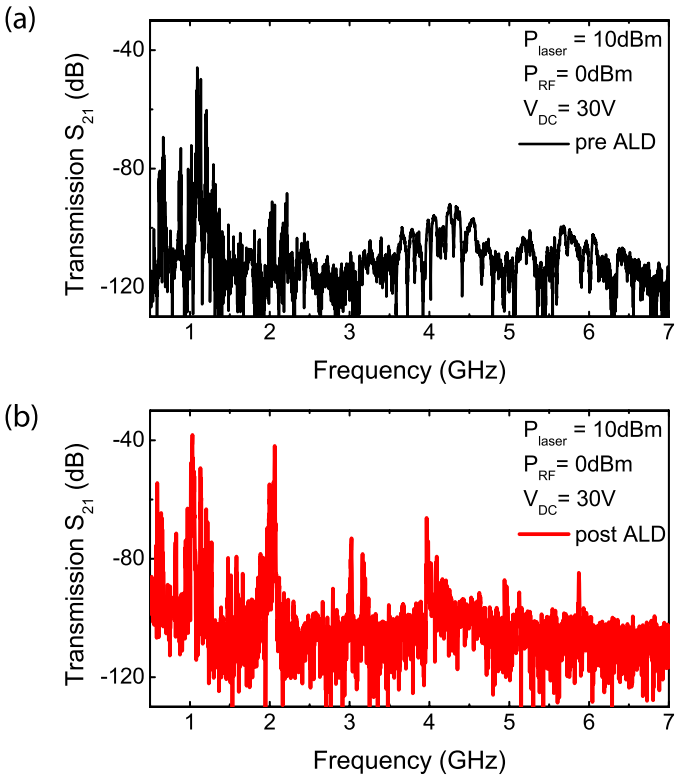


Fig. 4. Comparison of the modulator transmission spectrum (a) pre ALD and (b) post ALD. The most pronounced transduction enhancement is recorded at 2.05GHz (47dB improvement).

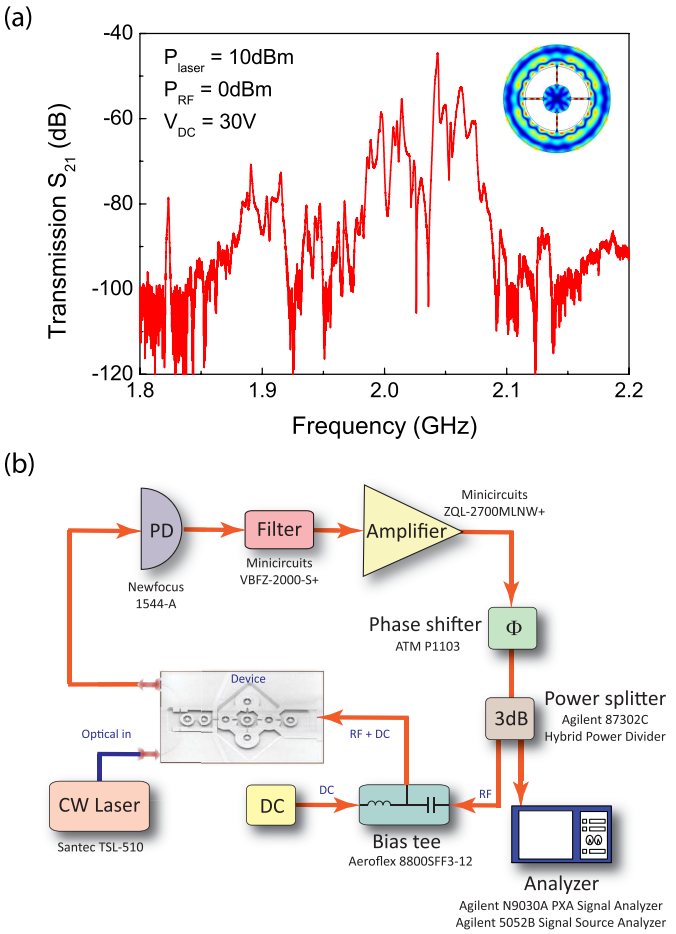


Fig. 5. (a) Transmission spectrum of the device measured with the introduction of a band-pass filter to select mechanical modes around 2GHz. Inset: Finite Element Method (FEM) simulated mechanical resonance mode shape at 2.047GHz. (b) Schematic of the 2.05GHz oscillator loop.

spatial overlap of the optical modes in the waveguide and the resonator on account of reduced waveguide-resonator air gap post ALD.

### *B. Characterization of the Mechanical Spectrum*

To measure the transmission for the acousto-optic modulator, we replace the optical power meter with a high bandwidth photoreceiver (Newfocus 1544-A). Motion is actuated in the opto-mechanical resonator by connecting the electrode to port 1 of a network analyzer and a DC bias voltage using a bias tee. The output of the photodetector is connected to port 2 of the network analyzer. Figure 4 shows the transmission response measured at the network analyzer. The signal boost at higher frequencies is clear and the enhancement is most prominent for the mechanical mode with frequency 2.1GHz, which shows 5 orders of magnitude improvement in insertion loss (-88dB pre ALD; −41dB post ALD). Mass loading of the resonator and the coupling beams due to ALD results in degradation of the mechanical Q from 2,300 prior to ALD to 800 post ALD, similar to that observed by Akgul et al. [7].

## IV. Opto-Acoustic Oscillator (OAO)

To select the second order compound radial expansion mode at 2.05GHz and suppress the other mechanical modes of the device, we use a band-pass filter (Mini-circuits VBFZ-2000-S+). Figure 5 (a) shows the RF transmission spectrum measured by introducing the filter at frequencies in the vicinity of the second order compound radial expansion mode at 2.05GHz (Figure 5 (a) inset), which exhibits a phase transition through 0°. The other spurious peaks are attributed to imperfections in the beam lengths due to fabrication variations. The tallest peak at 2.047GHz corresponds to the mechanical mode with best momentum balance. The second tallest peak at 2.067GHz has a frequency separation of 20MHz from this mode and has 8dB larger insertion loss. Since the oscillator loop locks to a single mechanical mode, an oscillator operating at 2.047GHz will not be affected by the other mechanical modes.

To reduce the insertion loss, we choose a higher laser power (15dBm) and a larger DC bias for the device (45V). We operate the 2.05GHz mechanical resonance in a feedback loop using an amplifier with a gain of 25dB (Mini-circuits ZQL-2700MLNW+) and a phase shifter. The amplifier overcomes the insertion loss introduced by the device (acousto-optic modulator) to meet the unity gain condition required for start-up of oscillations. The phase shifter ensures that the phase around the loop is a multiple of $2\pi$. Figure 5 (b) shows a schematic of the oscillator feedback loop.

Figure 6 shows the RF spectrum and phase noise of the oscillations at 2.05GHz. The oscillation signal phase noise

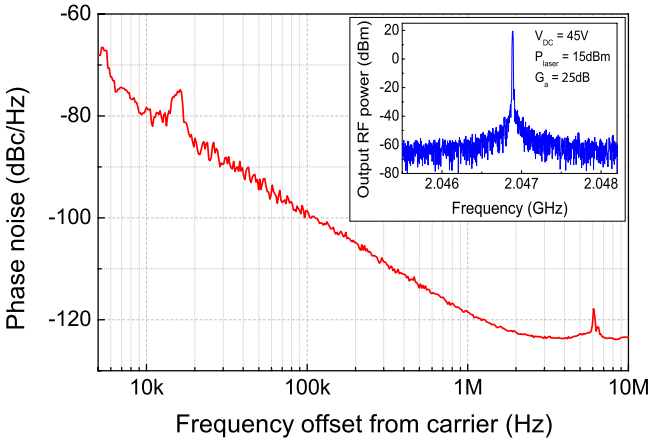


Fig. 6. Phase noise of the oscillations at 2.05GHz, with −80dBc/Hz noise at 10kHz offset from carrier. Inset: RF spectrum of oscillations at 2.05GHz. The phase noise is measured using an Agilent 5052B signal source analyzer.

at 10kHz offset from carrier is −80dBc/Hz. We measure the phase noise using an Agilent 5052B signal source analyzer. Using a low noise amplifier results in lack of $1/f^3$ slopes down to 5kHz offset from carrier in the phase noise plot unlike [15]. The $1/f^2$ corner frequency is observed to be ≈2MHz, which is consistent with the measured mechanical Q of 800.

The mechanical motion of the ring resonator interrogated optically leads to a shift in its optical resonance frequency, and hence leads to modulation of the light coupled to the resonator. The optical resonance shape is Lorentzian (see Figure 3 (b)), and therefore the modulation is non-linear. This results in generation of multiple harmonics of the fundamental oscillation frequency, as observed earlier in opto-mechanical oscillators which function based on the same modulation scheme [19], [20]. Figure 7 (a) shows measured harmonics all the way up to 16.4GHz.

We use band-pass filters to select the oscillation harmonics at 4.1GHz (VBFZ-4000+) and 6.15GHz (VBFZ-6260+) and measure their phase noise. The signals at these frequencies are expected to have the same noise signature as the fundamental harmonic at 2.05GHz. The non-linear shape of the optical resonance serves as an ideal frequency multiplier in this case, and hence the noise of all the higher oscillation harmonics of order $n$ are expected to be worse than the phase noise of the 2.05GHz signal by $20log_{10}(n)$dB. The phase noise at 4.1GHz and 6.15GHz signals follows this trend as seen in Figure 7 (b).

## V. OAO Phase Noise Model

To model the phase noise of the OAO, we follow a methodology similar to conventional noise analysis in PLL systems [21] and optoelectronic oscillators [14]. The fundamental noise contributions in the OAO arise primarily from the thermal noise, the photodetector shot noise, noise contributed by the amplifier, and the laser's intensity noise. For the sake of noise analysis, we break the loop and write down an expression for the noise-to-signal ratio at the output of the amplifier.

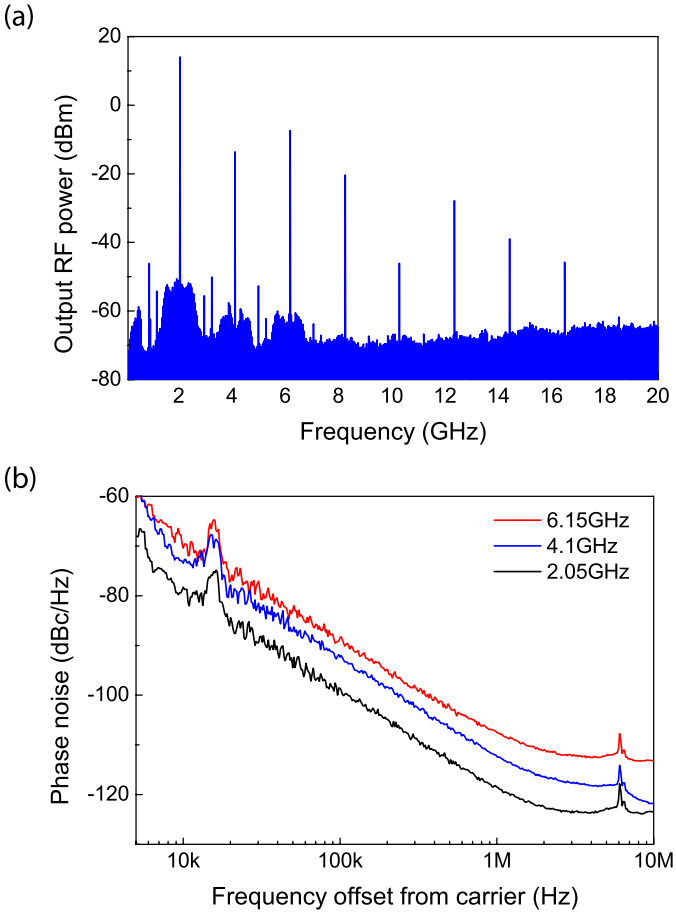


Fig. 7. (a) Plot showing various harmonics of the fundamental oscillations at 2.05GHz. The signal power at 16.4GHz is measured to be −45dBm. (b) Comparison of phase noise of the oscillations at 2.05GHz, 4.1GHz and 6.15GHz. The phase noise for the higher harmonics of order n is worse than the fundamental by 20log(n)dB. The RF oscillation signal power at the phase noise analyzer is maintained to be the same for all curves (-5dBm) using RF attenuators.

The noise spectral density at the input terminal of the amplifier can be written down as (in units of $V^2/Hz$):

$$\rho_{n,in} = S_x(\Omega_{mech})\, H_{opt} P_{CW} g_{OM} G_{PD}^2 + 2e\Psi P_{CW} R_{PD} + N_{RIN} I_{ph}^2 R_{PD} \quad (1)$$

The first term in the RHS is the thermal Brownian noise (details in Appendix A) amplified by the photodetector gain ($G_{PD}$). The second and third terms are the detector shot noise and the laser's intensity noise respectively. For benchtop tunable lasers, the intensity noise is negligibly small compared to the thermal noise and the shot noise and can be safely ignored. The optical power at the input of the photodetector is denoted by $P_{CW}$, $\Psi$ is the responsivity of the photodetector, $I_{ph} = \Psi P_{CW}$ is the photocurrent across the load resistor of the photodetector, $R_{PD}$, and $N_{RIN}$ is the relative intensity noise (RIN) of the input laser. The symbol $e$ denotes the elementary positive charge, $\approx 1.6*10^{-19}C$. The thermal noise component at the output of the amplifier is obtained by scaling the input thermal noise by the amplifier noise factor. The total noise at the output of the amplifier can then be expressed in terms of

the noise factor ($F$) and the gain ($G_A$) as:

$$\rho_{n,out} = G_A^2\Big(FS_x\left(\Omega_{mech}\right)H_{opt}P_{CW}g_{OM}G_{PD}^2 + 2e\Psi P_{CW}R_{PD} + N_{RIN}I_{ph}^2R_{PD}\Big) \quad (2)$$

This yields the following expression for noise-to-signal ratio at the output of the amplifier:

$$\delta = \frac{\rho_{n,out}}{P_{sig}} \quad (3)$$

Following the derivation in [14], the full width at half maximum (FWHM) linewidth of the oscillation signal is then obtained as:

$$\Delta f_{FWHM} = \frac{\delta}{2\pi\tau^2} \quad (4)$$

where $\tau = \frac{2Q_{mech}}{\Omega_{mech}} + \frac{2Q_{opt,tot}}{\omega_p}$ is the delay in the oscillation loop, due to circulation of photons inside the optical cavity $\left(\frac{2Q_{opt,tot}}{\omega_p}\right)$ and the filter response of the mechanical resonance $\left(\frac{2Q_{mech}}{\Omega_{mech}}\right)$. With an expression for the oscillation linewidth in place, we model the phase noise [24] for the OAO in the $\frac{1}{f^2}$ regime as follows:

$$L\left(\Delta f\right)_{\frac{1}{f^2}} = 10log_{10}\left(\frac{1}{\pi}\frac{\Delta f_{FWHM}}{\left(\Delta f_{FWHM}\right)^2 + \left(\Delta f\right)^2}\right) \quad (5)$$

Flicker noise sources in the amplifier stages in the OAO contribute to $\frac{1}{f^3}$ dependence of phase noise on frequency. If $f_3$ denotes the corner frequency for $\frac{1}{f^3}$ noise in the phase noise spectrum, the phase noise in this regime can be expressed as follows:

$$L\left(\Delta f\right)_{\frac{1}{f^3}} = 10log_{10}\left(\frac{1}{\pi}\frac{\Delta f_{FWHM}}{\left(\Delta f_{FWHM}\right)^2 + \left(\Delta f\right)^2}\frac{f_3}{\Delta f}\right) \quad (6)$$

The noise floor of the phase noise plot can then be expressed as:

$$L\left(\Delta f\right)_{noisefloor} = 10log_{10}\left(\frac{1}{\pi}\frac{\Delta f_{FWHM}}{\left(\Delta f_{FWHM}\right)^2 + \left(\frac{\Omega_{mech}}{2Q_{mech}}\right)^2}\right) \quad (7)$$

The comparison of the phase noise calculated using this model to measured phase noise is shown in Figure 8. The value of $f_3$ is empirically determined from the measured phase noise spectrum. The Newfocus 1544-A photoreceiver used in the experiments reported in earlier sections has a conversion gain of 800V/W and Noise Equivalent Power (NEP) of 24pW/$\sqrt{Hz}$. The bench-top Santec TSL-510 laser used in this experiment has a relative intensity noise (RIN) of −145dB/Hz. This implies that the ultimate signal-to-noise ratio for the oscillation signal will be −145dB/Hz. The phase noise spectra recorded have phase noise values higher than −145dBc/Hz and as expected, the laser RIN is an insignificant noise source. Substituting experimental parameters used in the setup, the electronic shot noise in the system ($1.44*10^{-20}V^2/Hz$) is orders of magnitude larger than the thermal noise ($3.19*10^{-25}V^2/Hz$). The dominant contribution to the noise spectral density in equation 1 thus comes from the shot noise in the photodetector, which is directly proportional to the input optical power. To design an oscillator with lower phase noise, we need to use a photoreceiver with a larger signal-to-noise-ratio (SNR), and hence lower NEP. Also, it is desirable to have an RF bandwidth >2GHz and a large gain and for the photoreceiver, that would allow for reduced optical input power and hence lower shot noise. The R604-APD avalanche photodetector manufactured by Discovery Semiconductors provides a single ended conversion gain of 12,000V/W and a 3-dB bandwidth of 7GHz, with an NEP <2.4pW/$\sqrt{Hz}$. Using this photoreceiver, we obtain a phase noise floor of −137dBc/Hz as seen in Figure 8. To provide sufficient gain in the feedback loop, we have to use an additional amplifier (Minicircuits ZRL-2400LN with a gain of 25dB, alongwith a 20dB attenuator to avoid gain saturation in the amplifier chain), which shifts the 1/f$^3$ corner frequency to ≈200kHz. The optical input power at the photodetector was measured to be 200$\mu$W for the R604-APD, and 10mW for the 1544-A photoreceiver. A larger optical power was not used while operating the oscillator with the R604-APD since this avalanche photodetector is a high sensitivity detector that is typically used with optical input powers not exceeding −10dBm. By significantly reducing the optical power used to operate the oscillator using a high-gain photoreceiver, we are successfully able to lower the shot noise in the oscillator loop, thus achieving 15dB lower far-from-carrier phase noise.

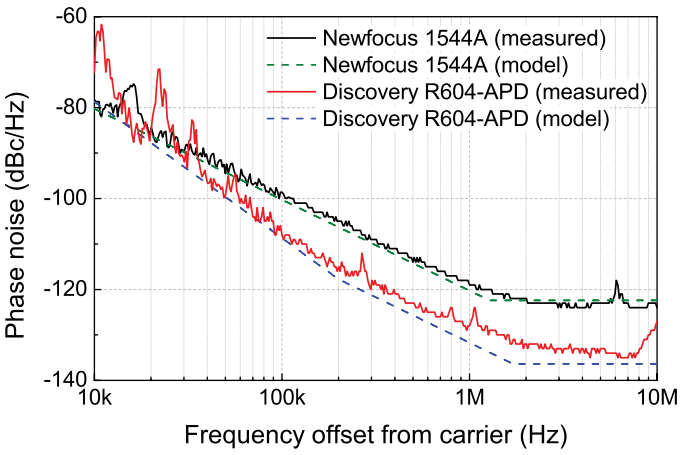


Fig. 8. Comparison of measured phase noise for oscillation signal at 2.05GHz to phase noise calculated using the model presented here. The black curve is the phase noise recorded using a NewFocus 1544A photoreceiver and the red curve is obtained using a Discovery Semiconductors R604-APD avalanche photodetector. The green and blue dashed curves are the calculated phase noise performance using the phase noise model. The model clearly fits well to the measured phase noise numbers.

## VI. Phase Noise Variation With Laser Detuning

The RF signal generated by the photodetector depends on the detuning of the laser wavelength from the cavity optical resonance wavelength (see Appendix A). As a result, the phase noise of the oscillation signal also varies with the detuning. Figure 9 (a) shows phase noise spectra for the oscillator recorded at various relative detuning values measured using the R604-APD photoreceiver. Relative detuning is defined as

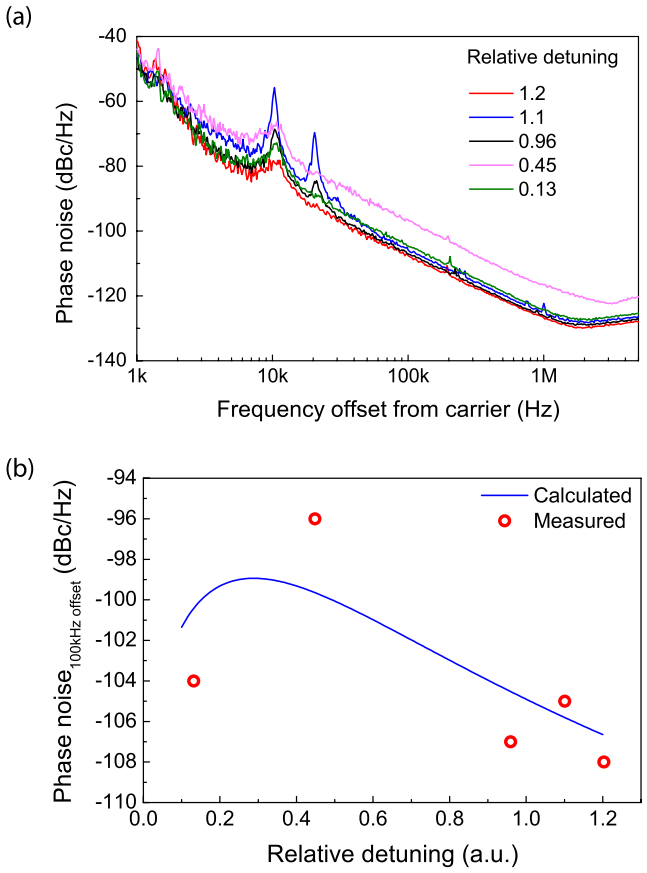


Fig. 9. (a) Variation of phase noise for the oscillation signal at 2.05GHz for various relative detuning values. A DC voltage of 35V was used to operate the oscillator. (b) Phase noise at 100kHz offset from carrier measured for various relative detuning values.

$\frac{\Delta_0}{2\delta}$, where $\Delta_0 = \omega_0 - \omega_p$ is the detuning of the pump laser frequency $\omega_p$ from the cavity optical resonance frequency $\omega_0$, and $\delta$ is the full-width-at-half-maximum (FWHM) linewidth of the cavity optical resonance. Figure 9 (b) compares the measured phase noise at 100kHz offset from the carrier with the calculated value of phase noise based on the model presented here. Based on this observed trend we conclude that it is desirable to choose a relative detuning value $\approx 1$ for the best phase noise performance.

## VII. Conclusion

A novel process flow realizing post-release photolithography on MEMS structures was developed to enable the design and fabrication of partial air gap transduced silicon MEMS resonators. A combination of partial air gap capacitive transduction and micromechanical displacement amplification was employed to enable a silicon MEMS opto-acoustic oscillator operating at 2.05GHz with RF power of 18dbm and phase noise of $-80$dBc/Hz at 10kHz offset from carrier. The device also benefits from the built-in opto-mechanical frequency multiplier, which yields high power harmonics of the oscillation signal all the way up to $-45$dBm signal power at 16.4GHz. The optical modulation serves as an ideal frequency multiplier, and the phase noise in the harmonics at 4.1 GHz and 6.15GHz are measured to be 6dB and 10dB worse than the noise at 2.05GHz as expected. The phase noise of these tones does not show any degradation due to the absence of an external mixer. We also presented a phase noise model that identifies the photodetector shot noise as the primary noise source, and based on these findings, we employed a lower noise avalanche photodetector, which yields a reduction in the phase noise floor by 15dB. The phase noise of the oscillator depends heavily on the optical detuning, and hence operating with a relative detuning $\approx 1$ is desirable for low phase noise operation. In addition to recent advances in nonlinear optics leading to photonic micro-resonator based X-band oscillators [25], [26], these results constitute one of the first MEMS resonator based frequency sources in the microwave X-band.

## Appendix A
## Thermal Brownian Noise Derivation

The power spectral density of the Brownian motion can be written as in equation 8 as follows:

$$S_x(\Omega_{mech}) = \sqrt{\frac{4k_B T Q_{mech}}{m_{eff}\Omega_{mech}^3}} \tag{8}$$

where $k_B$ is the Boltzman constant, $T$ is the ambient temperature, and $Q_{mech}, m_{eff}$ and $\Omega_{mech}$ are the quality factor (800), effective mass (calculated to be 59.3fg from COMSOL FEM eigenfrequency simulations) and frequency (2.05GHz) of the mechanical resonance respectively. The motion of the cavity leads to modulation of the transmitted optical power at the output of the device, $\sqrt{\langle P_{mod}^2 \rangle} = \frac{dT}{dr} P_{CW} S_x(\Omega_{mech})$. The scale factor, $\frac{dT}{dr}$, denotes the change in optical transmission ($T$) with radial displacement ($r$). Note that we can express $\frac{dT}{dr}$ in terms of the opto-mechanical coupling coefficient, $g_{OM}$ as $\frac{dT}{dr} = \frac{dT}{d\omega_0}\frac{d\omega_0}{dr} = H_{opt} g_{OM}$. $H_{opt}$ is the cavity transfer function expressed as in equation 9 [22]:

$$H_{opt} = \sqrt{\frac{4\kappa_{ext}^2 \kappa_{int}^2 \Delta_0^2}{\left[\Delta_0^2 + \left(\frac{\kappa_{tot}}{2}\right)^2\right]^4}} \tag{9}$$

where $\Delta_0 = \omega_0 - \omega_p$ is the static detuning of the laser frequency ($\omega_p$) with respect to the optical cavity resonance frequency ($\omega_0$), $\kappa_{ext}$ is the rate associated with coupling of photons to the optical cavity, and $\kappa_{int}$ and $\kappa_{tot}$ are the intrinsic and loaded cavity photon decay rates respectively.

The power noise spectral density at the output of the photodetector can then be expressed as follows:

$$\begin{aligned}\sqrt{\langle P_{n,PD_{out}}^2 \rangle} &= \sqrt{\langle P_{mod}^2 \rangle} G_{PD}^2 \\ &= H_{opt} g_{OM} P_{CW} S_x(\Omega_{mech}) G_{PD}^2\end{aligned} \tag{10}$$

The thermal noise contribution from the mechanical resonator thus calculated yields 389pW/$\sqrt{Hz}$, which is significantly larger than the NEP of the photodetector used in the system.

TABLE I
OSCILLATOR FIGURE OF MERIT (FOM) COMPARISON

| Reference | Oscillation Frequency (GHz) | Phase noise at 100kHz offset (dBc/Hz) | DC Power Consumption (mW) | FOM (dBc/Hz) |
|---|---|---|---|---|
| [9] | 1.9 | -120 | 0.3 | -210 |
| [5] | 0.06 | -135 | 0.35 | -195 |
| [11] | 3.4 | -140 | 20 | -216 |
| **This work** | 2.05 | -110 | 740 | -167 |

## APPENDIX B
## COMPARISON OF THE OPTO-ACOUSTIC OSCILLATOR TO STATE-OF-THE-ART

A popular figure of merit (FOM) for oscillators summarizes the important performance parameters – phase noise $L(\Delta f)$, oscillator frequency $f_{osc}$ and DC power consumption $P_{DC}$ – to make a fair comparison:

$$FOM = L(\Delta f) + 20log_{10}\left(\frac{\Delta f}{f_{osc}}\right) + 10log_{10}\left(\frac{P_{DC}}{1mW}\right) \quad (11)$$

The second term neutralizes the effect of the offset frequency $\Delta f$ while taking the oscillator frequency into account. $P_{DC}$ is measured in milli-Watts (mW). Table I compares the performance of the OAO presented here to other MEMS oscillator technologies. The FOM for our 2.05GHz OAO is completely dominated by the oscillator's DC power consumption. The large power consumption comprises of the laser power consumption (166mW), photodetector (250mW) and RF amplifier (320mW). The Santec TSL-510 laser used in our experiments has a power efficiency of 6%. Low power laser and photodetector development is an active area of research, and power scaling of on-chip lasers and detectors should enable an OAO with improved FOM.

## ACKNOWLEDGMENT

The authors would like to express their thanks to Dr. Suresh Sridaran of Avago Technologies for initial fabrication of devices, and Dr. Shantanu Rajwade and Dr. Laura Fegely of Cornell University, and Noah Clay at Cornell NanoScale Science and Technology Facility for invaluable tips and suggestions to design the fabrication process flow.

## REFERENCES

[1] S. Tallur and S. A. Bhave, "Monolithic 2 GHz electrostatically actuated MEMS oscillator with opto-mechanical frequency multiplier," in *Proc. 17th Int. Conf. Solid-State Sens., Actuators, Microsyst.*, 2013, pp. 1472–1475.

[2] J. T. M. van Beek and R. Puers, "A review of MEMS oscillators for frequency reference and timing applications," *J. Micromech. Microeng.*, vol. 22, no. 1, pp. 013001-1–013001-35, 2012.

[3] C. T.-C. Nguyen, "MEMS technology for timing and frequency control," *IEEE Trans. Ultrason., Ferroelectr., Freq. Control*, vol. 54, no. 2, pp. 251–270, Feb. 2007.

[4] G. K. Ho, K. Sundaresan, S. Pourkamali, and F. Ayazi, "Temperature compensated IBAR reference oscillators," in *Proc. 19th IEEE Int. Conf. Micro Electro Mech. Syst. (MEMS)*, Jan. 2006, pp. 910–913.

[5] Y.-W. Lin, S.-S. Li, Z. Ren, and C. T.-C. Nguyen, "Low phase noise array-composite micromechanical wine-glass disk oscillator," in *IEEE Int. Electron Devices Meet. (IEDM) Tech. Dig.*, Dec. 2005, pp. 281–284.

[6] L.-W. Hung, Z. A. Jacobson, Z. Ren, A. Javey, and C. T.-C. Nguyen, "Capacitive transducer strengthening via ALD-enabled partial-gap filling," in *Solid-State Sens., Actuators, Microsyst. Workshop Tech. Dig.*, 2008, pp. 208–211.

[7] M. Akgul *et al.*, "Oscillator far-from-carrier phase noise reduction via nano-scale gap tuning of micromechanical resonators," in *Proc. Solid-State Sens., Actuators, Microsyst. Conf.*, 2009, pp. 21–25.

[8] S. Tallur, T. J. Cheng, S. Sridaran, and S. A. Bhave, "Motional impedance analysis: Bridging the 'Gap' in dielectric transduction," in *Proc. IEEE Int. Freq. Control Symp.*, May 2011, pp. 135–138.

[9] B. P. Otis and J. M. Rabaey, "A 300-$\mu$W 1.9-GHz CMOS oscillator utilizing micromachined resonators," *IEEE J. Solid-State Circuits*, vol. 38, no. 7, pp. 1271–1274, Jul. 2003.

[10] S. Rai *et al.*, "A 1.5 GHz CMOS/FBAR frequency reference with $\pm$10ppm temperature stability," in *Proc. IEEE Int. Freq. Control Symp. Joint 22nd Eur. Freq. Time Forum*, Apr. 2009, pp. 385–387.

[11] R. Ruby *et al.*, "Positioning FBAR technology in the frequency and timing domain," *IEEE Trans. Ultrason., Ferroelectr., Freq. Control*, vol. 59, no. 3, pp. 334–345, Mar. 2012.

[12] C. Zuo, J. Van der Spiegel, and G. Piazza, "1.05 GHz MEMS oscillator based on lateral-field-excited piezoelectric AlN resonators," in *Proc. IEEE Int. Freq. Control Symp., Joint 22nd Eur. Freq. Time Forum*, Apr. 2009, pp. 381–384.

[13] C. Zuo, J. Van der Spiegel, and G. Piazza, "Switch-less dual-frequency reconfigurable CMOS oscillator using one single piezoelectric AlN MEMS resonator with co-existing S0 and S1 Lamb-wave modes," in *Proc. IEEE 24th Int. Conf. Micro Electro Mech. Syst. (MEMS)*, Jan. 2011, pp. 177–180.

[14] X. S. Yao and L. Maleki, "Optoelectronic microwave oscillator," *J. Opt. Soc. Amer. B*, vol. 13, no. 8, pp. 1725–1735, 1996.

[15] S. Sridaran and S. A. Bhave, "1.12 GHz opto-acoustic oscillator," in *Proc. IEEE 25th Int. Conf. Micro Electro Mech. Syst. (MEMS)*, Jan./Feb. 2012, pp. 644–647.

[16] S. Tallur and S. A. Bhave, "Electromechanically induced GHz rate optical frequency modulation in silicon," *IEEE Photon. J.*, vol. 4, no. 5, pp. 1474–1483, Oct. 2012.

[17] S. Tallur and S. A. Bhave, "Comparison of f-Q scaling in wineglass and radial modes in ring resonators," in *Proc. IEEE 26th Int. Conf. Micro Electro Mech. Syst. (MEMS)*, Jan. 2013, pp. 777–780.

[18] W.-C. Li *et al.*, "Digitally-specified micromechanical displacement amplifiers," in *Proc. Int. Solid-State Sens., Actuators, Microsyst. Conf. (TRANSDUCERS)*, Jun. 2009, pp. 781–784.

[19] S. Tallur, S. Sridaran, and S. A. Bhave, "A monolithic radiation-pressure driven, low phase noise silicon nitride opto-mechanical oscillator," *Opt. Exp.*, vol. 19, no. 24, pp. 24522–24529, 2011.

[20] T. O. Rocheleau *et al.*, "Enhancement of mechanical Q for low phase noise optomechanical oscillators," in *Proc. IEEE 26th Int. Conf. Micro Electro Mech. Syst. (MEMS)*, Jan. 2013, pp. 118–121.

[21] V. Kroupa, "Noise properties of PLL systems," *IEEE Trans. Commun.*, vol. 30, no. 10, pp. 2244–2252, Oct. 1982.

[22] J. Rosenberg, Q. Liu, and O. Painter, "Static and dynamic wavelength routing via the gradient optical force," *Nature Photon.*, vol. 3, pp. 478–483, Jul. 2009.

[23] D. B. Leeson, "A simple model of feedback oscillator noise spectrum," *Proc. IEEE*, vol. 54, no. 2, pp. 329–330, Feb. 1966.

[24] S. Tallur, S. Sridaran, S. A. Bhave, and T. Carmon, "Phase noise modeling of opto-mechanical oscillators," in *Proc. IEEE Int. Freq. Control Symp. (FCS)*, Jun. 2010, pp. 268–272.

[25] M. Tomes and T. Carmon, "Photonic micro-electromechanical systems vibrating at *X*-band (11-GHz) rates," *Phys. Rev. Lett.*, vol. 102, no. 11, pp. 113601-1–113601-4, 2009.

[26] H. Lee *et al.*, "Chemically etched ultrahigh-Q wedge-resonator on a silicon chip," *Nature Photon.*, vol. 6, pp. 369–373, May 2012.

**Siddharth Tallur** received the B.Tech. and Ph.D. degrees in electrical engineering from IIT Bombay, Mumbai, India, and Cornell University, Ithaca, NY, USA, in 2008 and 2014, respectively. Prior to joining Cornell University, he was serving as a Business Analyst at the global strategy consulting firm A.T. Kearney Ltd., Mumbai. He was a recipient of the Best Student Paper Award at the 2012 IEEE Photonics Conference held in Burlingame, CA, USA, for his work on electromechanically induced optical frequency modulation, and was recognized by the U.S. Advisory Committee to the International Commission for Optics. He was also with the ApselLab at Cornell University, and has co-authored several papers on design and characterization of a low-power ultrawideband impulse radio transceiver. His thesis research on optomechanical oscillators and MEMS-aided photonics applications has earned him the Cornell University ECE Director's Best Thesis Research Award in 2013. He is currently with Analog Devices Inc., Norwood, MA, USA, as a MEMS Sensor Platform Development Engineer for inertial sensor products.

**Sunil A. Bhave** (S'99–M'04–SM'10) received the B.S. and Ph.D. degrees in electrical engineering and computer science from the University of California at Berkeley, Berkeley, CA, USA, in 1998 and 2004, respectively. Since 2004, he has been with Cornell University, Ithaca, NY, USA, where he is currently an Associate Professor with the School of Electrical and Computer Engineering. His research interests include exploring, understanding, and exploiting interdomain coupling in optomechanical, spin-acoustic, and atom-MEMS systems to design inertial sensors, clocks, and field-programmable microwave chipsets. He was a recipient of the National Science Foundation Early CAREER Development Award in 2007, the Defense Advanced Research Projects Agency Young Faculty Award in 2008, and the IEEE Ultrasonics Young Investigator Award in 2014. Along with his students, he has been awarded the Roger A. Hakan Best Paper Award at the International Electron Devices Meeting in 2007, and the Student Paper Competition Award at the IEEE International Ultrasonics Symposium in 2009 and the IEEE Photonics Conference in 2012.